Cofilin promotes actin turnover and flexibility to drive coordinated cell movements *in vivo*

Ana Maria do Carmo[1, 2], Ji Hong Sayo[1, 2, 3], and Rodrigo Fernandez-Gonzalez[1, 2, 4, 5, *]

[1] Institute of Biomedical Engineering, University of Toronto, Toronto, ON, M5S 3G9, Canada.

[2] Translational Biology and Engineering Program, Ted Rogers Centre for Heart Research, University of Toronto, Toronto, ON, M5G 1M1, Canada.

[3] Division of Engineering Science, University of Toronto, Toronto, ON, M5S 1A4, Canada.

[4] Department of Cell and Systems Biology, University of Toronto, Toronto, ON, M5S 3G5, Canada.

[5] Developmental and Stem Cell Biology Program, The Hospital for Sick Children, Toronto, ON, M5G 1X8, Canada.

[*] Corresponding author:

email: rodrigo.fernandez.gonzalez@utoronto.ca

phone: 416-978-7368

Abstract

Embryos display a striking ability to repair wounds rapidly, with no inflammation or scarring. Embryonic wound healing is driven by the collective movement of the cells adjacent to the wound. The cells at the wound edge polarize actin and the molecular motor non-muscle myosin II, forming a supracellular cable around the wound that generates force and coordinates cell movements to close the lesion. Actin network contraction has been associated with the disassembly of the actin filaments that form the network. We found that the actin-severing protein cofilin and its co-factor Aip1 accumulated at the edge of epidermal wounds in *Drosophila* embryos. Reducing cofilin activity slowed down wound closure by 26%, indicating that cofilin is necessary for rapid wound healing. Using quantitative microscopy, we showed that cofilin controls F-actin turnover at the wound edge, but not F-actin polarity or contractile force generation. Combining genetic and pharmacological manipulations, we found that F-actin turnover at the wound edge must be tightly regulated for wounds to close rapidly. Computational modelling suggested that cofilin may contribute to rapid wound repair by maintaining a flexible actin network at the wound edge. Consistent with this model, fluorescence fluctuation analysis revealed that F-actin networks at the wound edge were significantly more rigid when we reduced cofilin activity. Together, our results indicate that cofilin promotes F-actin turnover at the wound edge to maintain a flexible actin network and facilitate rapid contraction and wound healing.

Introduction

Wound healing in embryos occurs rapidly, without inflammation or scarring[1,2]. Embryonic wound repair is a conserved morphogenetic process driven by the collective migration of the cells around the wound. Upon wounding, actin and the molecular motor non-muscle myosin II become polarized in the cells immediately adjacent to the wound, forming a supracellular actomyosin cable at the wound edge[3-6]. The actomyosin cable contracts, coordinating cell movements to draw the wound closed[6-10].

The architecture and organization of F-actin networks can affect their contraction[11,12]. Crosslinking proteins connect different actin filaments and thus can modulate force transmission throughout a network[13]. The effect of crosslinkers on F-actin networks is influenced by filament density and length, with longer filaments being more heavily crosslinked[14]. The presence of crosslinkers also alters network properties, making them more rigid[15,16]. A high crosslinker density has been associated with reduced contractility[17,18], likely because crosslinkers hinder F-actin bundle bending[19], which is an important symmetry breaking mechanism that contributes to actomyosin contraction both *in vitro*[13] and *in vivo*[20].

Actin filament disassembly is also critical for actin network contraction. Stabilization of actin filaments during cytokinesis in budding yeast slows down the scission of the two daughter cells[21]. Similarly, F-actin severing is key for the contraction of the actin networks that drive cellularization of the *Drosophila* embryo[22], gastrulation[23], or wound healing in pupal tissues[24]. Consistent with a role for actin disassembly in embryonic wound closure, F-actin levels at the wound edge decrease as the wound repairs[8], and F-actin stabilization slows down wound healing[25].

Cofilin is one of the main actin-severing proteins[26]. Cofilin binds preferentially to the pointed end of actin filaments[27], where monomer removal dominates. Cofilin binding induces a change in filament conformation that increases the flexibility of the cofilin-decorated segment[28,29]. Thus, cofilin binding creates a boundary between the flexible (cofilin-decorated) and the rigid (non-decorated) ends of the filament that renders the filament susceptible to severing when thermal fluctuations occur[28,30,31]. Cofilin is regulated by phosphorylation: the serine/threonine kinase LIM domain kinase (LIMK) phosphorylates cofilin and inhibits actin binding, thus inactivating cofilin[32,33]. Whether cofilin regulates actin dynamics during embryonic wound healing is currently unknown.

Results

Cofilin is necessary for rapid embryonic wound healing

To investigate if cofilin may be implicated in embryonic wound healing, we examined the localization of an endogenously-tagged form of cofilin[34,35] during wound repair in embryos of the fruit fly *Drosophila melanogaster*. In the intact epidermis, cofilin localized predominantly to the nuclei of epidermal cells, with an additional cytosolic pool (Fig. 1A). Strikingly, there was little-to-no accumulation of cofilin at cell-cell junctions. Upon wounding, cofilin accumulated at the edge of the wound, with cofilin levels at the wound margin increasing by 11 ± 1% (mean ± standard deviation, SD) (Fig. 1A-B). A GFP-tagged form of the cofilin cofactor AIP1[36] was also largely absent from cell junctions in the intact epidermis, but similar to cofilin, AIP1 accumulated at the wound edge by 27 ± 12%. (Fig. 1C-D). Thus, our results suggest that cofilin may control actin dynamics to drive rapid embryonic wound repair.

Cofilin is necessary for cellularization of the *Drosophila* embryo[22] and for gastrulation[23]. Thus, to investigate if cofilin is necessary for rapid embryonic wound healing, we established a method to reduce cofilin activity while bypassing early embryonic development. We used the UAS-Gal4 system[37] to overexpress LIMK after gastrulation, using *daughterless-Gal4* [38] as the driver. To test if LIMK overexpression reduced cofilin activity, we fixed control embryos and embryos overexpressing LIMK 10-11 hours after egg laying, and we stained the embryos with antibodies against total cofilin and phospho-cofilin (P-cofilin), the inactive form of cofilin[22] (Fig. S1A-B). LIMK overexpression resulted in a 47% increase in the ratio of P-cofilin to total cofilin (P = 0.04, Fig. S1C). Thus, our results indicate that LIMK overexpression inactivates cofilin in the *Drosophila* embryonic epidermis.

To determine if cofilin contributes to rapid embryonic wound healing, we quantified the dynamics of wound closure in embryos overexpressing LIMK (Fig. 2A-B, Video S1). Embryos also expressed GFP:UtrophinABD[39], a fluorescent F-actin reporter. Reduced cofilin activity was associated with a slower wound healing response, as demonstrated by a slower reduction of the wound perimeter over time (Fig 2C). To quantify the delay in wound repair, we fitted exponential decays to the wound perimeter *vs.* time curves and used the decay constant as a metric for the rate of wound healing[40]. We found that reducing cofilin activity slowed down wound closure by

26% (P = 0.02, Fig. 2D). Together, our results show that cofilin activity is necessary for rapid embryonic wound repair.

Cofilin promotes F-actin turnover at the wound edge

To investigate the mechanisms by which cofilin contributes to rapid wound healing, we quantified F-actin fluorescence around the wound. Mean F-actin levels at the wound edge increased by 66 ± 17% in controls over the first 45 min after wounding (P = 0.0002, Fig. 2A, E). Reducing cofilin activity did not affect the polarization of F-actin to the wound edge, with F-actin levels increasing by 67 ± 10% in LIMK-overexpressing embryos (P = 0.0006, Fig. 2B, E). The polarization of actin to the wound edge remained unaffected by reducing cofilin activity when we compared wounds of similar perimeters (Fig. 2F). Similarly, mean myosin levels at the wound edge in embryos expressing a GFP-tagged form of the myosin regulatory light chain (encoded for by the *sqh* gene in *Drosophila*)[41] were not affected by reducing cofilin activity (Fig. S2A-D). In contrast, total F-actin at the wound edge decreased faster in control embryos than in embryos with reduced cofilin activity (Fig. 2G). However, the difference in total F-actin levels disappeared when we compared wounds of similar perimeter (Fig. 2H), suggesting that the slower reduction in total F-actin levels in embryos overexpressing LIMK is a consequence of the slower rate of wound closure. Overall, our results suggest that cofilin is dispensable for actomyosin polarization to the wound edge.

Cofilin flexibilizes and severs actin filaments, and thus, cofilin could regulate the dynamics of F-actin at the wound edge. To investigate this possibility, we used fluorescence recovery after photobleaching (FRAP) of the F-actin reporter GFP:UtrophinABD (Fig. 3A). We previously showed that the FRAP dynamics of GFP:UtrophinABD match the dynamics of other F-actin and monomeric actin reporters[25]. We photobleached a 2.7 x 2.7 μm^2 region on the actin cable around wounds that had closed to 50% of their maximum area. There were no significant differences in the mean fluorescence signal prior to photobleaching (Fig. 3B). We found that the degree of fluorescence recovery was lower in embryos with reduced cofilin activity when compared to controls (Fig. 3C): the percent of initial signal recovered (the mobile fraction) decreased by 25% in LIMK-overexpressing embryos with respect to controls (47 ± 15% *vs.* 62 ± 19%, respectively, P = 0.04, Fig. 3D). Reducing cofilin activity did not affect the rate of fluorescence recovery (the half-time, Fig. 3E). Thus, our experiments suggest that cofilin promotes F-actin turnover during embryonic wound healing.

Changes to tissue mechanics can disrupt wound healing responses[42]. To establish if the effect of cofilin on actin turnover and rapid wound repair is specific to the wound edge, we photobleached GFP:UtrophinABD in epidermal cell-cell junctions of embryos that had not been wounded (Fig. S3A). We found that there were no significant differences in the degree or rate of fluorescence recovery in the intact epidermis of embryos with reduced cofilin activity when compared to controls (Fig. S3B-E), consistent with the reduced levels of cofilin at cell-cell junctions (Fig. 1A). These results suggest that cofilin acts specifically at the wound edge during embryonic wound closure. We used laser ablation of cell-cell junctions to quantify the mechanical properties of the intact epidermis (Fig. S4A). We ablated single cell-cell junctions and measured the velocity of retraction of the ends of the severed junction, which is proportional to the tension released[43,44]. We did not find any effects of reducing cofilin activity on tension levels (Fig. S4B-C). To establish if the reduction in cofilin activity affects the viscoelastic properties of the epidermis, we modelled the results of the laser ablation experiments as the damped recoil of an elastic fibre using a Kelvin-Voigt mechanical equivalent circuit[44]. Using the model, we measured the asymptotic recoil distance, proportional to the tension-to-elasticity ratio, and a relaxation time proportional to the viscosity-to-elasticity ratio. There were no significant differences in either metric between control embryos and embryos with reduced cofilin activity (Fig. S4D). Together, our data show that cofilin acts specifically at the wound edge to promote F-actin turnover and rapid wound healing, with no significant effect on the global mechanics of the embryonic epidermis.

Cofilin controls myosin turnover but not tension at the wound edge

F-actin and myosin largely overlap at the wound edge[25]. To determine if reducing cofilin activity disrupts myosin dynamics during wound closure, we quantified myosin:GFP FRAP at the wound edge in controls and in embryos with reduced cofilin activity (Fig. S2E). We found that the mobile fraction of myosin decreased by 31% when cofilin activity decreased (44 ± 13% *vs.* 64 ± 15% in controls, $P = 0.03$, Fig. S2F-H), with no significant effect on the half-time of fluorescent recovery (Fig. S2I). Thus, our results show that cofilin promotes myosin turnover during embryonic wound closure.

Myosin stabilization is associated with increased tension at the wound edge[9]. To test if tension at the wound edge increases when cofilin activity decreases, we used laser ablation to

quantify the mechanical properties of the wound margin (Fig. S4E). We found no significant difference in the retraction velocity after ablation in embryos with reduced cofilin activity with respect to controls (Fig. S4F). Mechanical modelling further suggested that reducing cofilin activity did not affect tension or viscoelastic properties around the wound (Fig. S4G-H). Together, these data indicate that cofilin activity does not control force generation or viscoelasticity at the wound edge.

F-actin turnover must be precisely tuned for rapid wound healing

To determine if precise control of F-actin turnover is key for rapid wound repair, we tested whether increasing F-actin turnover rescued the wound healing phenotype in embryos with reduced cofilin activity. To increase F-actin turnover, we treated embryos with Latrunculin A (LatA), a toxin that sequesters actin monomers and promotes actin filament severing and depolymerization at low concentrations[45]. To determine if LatA treatment increased F-actin turnover, we conducted fluorescence recovery after photobleaching (FRAP) experiments in embryos expressing GFP:UtrophinABD and treated with 50% DMSO (controls) or with 750 µM of LatA in 50% DMSO (Fig. S5A). In FRAP experiments, embryos treated with LatA displayed an F-actin mobile fraction 33% higher than DMSO controls (54 ± 15% *vs.* 37 ± 6%, respectively, $P = 0.01$, Figure S5B-D), with no significant effects on the half-time of fluorescence recovery (Fig. S5E). Thus, LatA treatment is an effective method to destabilize F-actin. Increasing F-actin turnover was associated with a 67% reduction in the rate of wound closure ($P = 0.007$, Fig. 4A-B, E-F, Video S2). Consistent with our previous findings, reducing cofilin activity slowed down wound closure by 37% ($P = 0.02$, Fig. 4A, C, E-F, Video S2). Thus, both excessive and insufficient F-actin turnover are detrimental for rapid wound repair. Strikingly, increasing F-actin turnover with LatA in embryos with reduced cofilin activity rescued the rate of wound closure to control levels (Fig. 4A-F, Video S2). Overall, our results suggest that there is an optimal degree of F-actin turnover that is necessary for rapid wound repair.

Computational modelling suggests that cofilin may control F-actin rigidity to drive rapid wound healing

Cofilin and F-actin turnover could contribute to wound healing through effects on actin filament length[46-48], disassembly rate[27,49], filament severing[50], or F-actin rigidity[28,29]. To investigate how

different actin-associated parameters may affect embryonic wound healing, we developed a computational model of wound repair with molecular resolution. We implemented our model using Cytosim[51], which allows the simulation of actin networks containing filaments of tunable length, (dis)assembly rate and rigidity, and includes motor proteins, actin crosslinkers, and actin-severing proteins. Using Cytosim, we created an elliptical network of actin filaments to simulate the wound healing response (see Methods and Table S1). Parameter values were extracted from the literature (Table S1), with a final calibration step to obtain closure times consistent with our *in vivo* experiments. To examine how different parameters affected the contraction of the actin filament network, we individually varied initial filament length, actin filament disassembly rate, filament severing, and filament rigidity. Specifically, we investigated how potential effects of reducing cofilin activity (increasing initial filament length, reducing the rate of actin filament disassembly, reducing actin severing or increasing filament rigidity) would affect the rate of network contraction (Figs. 5A-D and S6A-D). The model predicted that reducing actin severing or increasing filament rigidity would both be detrimental for actomyosin network contraction (Fig. 5E-F, H-I, Videos S3 and S4). In contrast, increasing the length of actin filaments or reducing the rate of F-actin disassembly did not negatively impact the contraction of the network (Fig. S6A-J). Importantly, the model predicted that an increase in filament rigidity, but not a reduction of actin severing, would alter the shape of the network throughout its contraction, with flexible networks significantly more circular than rigid ones ($P < 0.01$, Fig. 5G, J). Thus, our model predicts that cofilin may control the rate of wound closure by inducing actin severing, with no effect on wound shape; or by promoting a flexible F-actin network and facilitating wound rounding as the wound closes.

Cofilin facilitates wound rounding associated with rapid repair

To distinguish between potential effects of cofilin on wound healing by affecting F-actin severing or rigidity, we measured the circularity of wounds in living embryos with reduced cofilin activity (Fig. 6A-B). Reducing cofilin activity was associated with a 10-19% reduction in circularity when comparing wounds at specific time points during wound closure ($P < 0.005$, Fig. 6C). Similarly, when comparing wounds of similar perimeter, reducing cofilin activity resulted in wounds that were 8-12% less circular than in controls ($P < 0.01$, Fig. 6D). These results are consistent with our model predictions if cofilin limits F-actin rigidity (Fig. 5J). Thus, our data suggest that cofilin

may contribute to rapid wound closure by maintaining a flexible F-actin network during embryonic wound healing. Notably, we found that increasing F-actin turnover with LatA treatment rescued wound circularity in embryos with reduced cofilin activity (Fig. S7A-E), suggesting a potential link between the effects of cofilin on F-actin turnover and rigidity.

Cofilin limits F-actin rigidity *in vivo*

Our results suggest that cofilin promotes F-actin turnover to limit F-actin rigidity and facilitate rapid embryonic wound healing. To establish if reducing cofilin activity affects F-actin rigidity *in vivo*, we measured the periodicity of F-actin fluorescence fluctuations at the wound edge[52-54]. Flexible actin filaments display greater (and thus less frequent) thermal fluctuations than rigid filaments[28] (Fig. 7A). Thus, if actin filaments were fluorescently labeled, the period of fluorescence fluctuations in a diffraction-limited spot should be greater for flexible F-actin networks than for rigid ones (Fig. 7A'). We quantified GFP:UtrophinABD fluctuations at the wound edge in control embryos and in embryos overexpressing LIMK using a spinning disk confocal microscope[55,56]. We selected wounds at 50% closure and acquired an image of the F-actin cable around the wound. After stopping the spinning disk, we selected pinholes overlaying the F-actin cable (Fig 7B). For each pinhole, we continuously collected 1600 images with 5 msec exposures (Fig. 7B, cutout). The amplitude of F-actin fluorescence fluctuations was dramatically reduced in fixed embryos with respect to living ones (Fig. 7C). To quantify the F-actin fluctuation period, we measured the autocorrelation of the fluorescence fluctuations (Fig. 7D). We found that the autocorrelation decay time was 23% lower in embryos with reduced cofilin activity with respect to controls ($P = 0.02$, Fig. 7-E), consistent with a reduction in fluctuation period and an increase in F-actin rigidity when cofilin activity decreased. Together, our results indicate that cofilin maintains a flexible F-actin network at the wound edge to facilitate rapid wound repair.

Discussion

Here we show that cofilin contributes to rapid wound repair by promoting F-actin turnover and flexibility specifically at the wound edge. The mechanisms that polarize cofilin to the wound margin remain unclear. F-actin polarization to the wound edge depends on calcium[57,58], reactive oxygen species[40], and signalling by the small GTPases Rap1[59] and Rho1[6,7]. Cofilin is a small protein that is able to freely diffuse[60]. Thus, the affinity of cofilin for F-actin could localize cofilin

at the wound margin. Alternatively, localized activation could mediate the polarization of cofilin. Cofilin activation is mediated by the phosphatase Slingshot[61], and Slingshot activity can be controlled by calcium[62], reactive oxygen species[63], or F-actin binding[61]. However, our data indicate that in the embryonic epidermis cofilin is largely active prior to wounding, suggesting that controlling localization, rather than activity, is key for the specific role that cofilin plays at the wound margin.

Our results demonstrate that cofilin also controls myosin turnover around the wound. We previously showed that myosin turnover is regulated by tension, with increasing tension slowing down myosin turnover[9,64]. This is possibly due to an increase in the myosin duty ratio (the fraction of time that the motor is bound to the filament) under high tension as a consequence of the slower release of ADP from the motor head[65]. Thus, our results suggest that at least two mechanisms control the dynamics of the actomyosin cytoskeleton around embryonic wounds: (1) cofilin mobilizes actin and myosin at the wound margin; and (2) tension stabilizes myosin motors. Cofilin-based mobilization may allow myosin motors or actin crosslinkers to dissociate from and reassociate with actin filaments[21], thus inducing productive contraction. This would be balanced by tension-based stabilization of motors and crosslinkers to ratchet contraction[10]. Whether myosin turnover and stabilization are coordinated is not understood. Cofilin binds and severs actin filaments in a tension-sensitive manner, with preferential binding and faster severing of relaxed filaments[66]. Tension at the wound edge increases as wound healing progresses[9], suggesting that cofilin-based actin severing may slow down as the wound closes, consistent with the slower turnover of myosin at later stages of tissue repair. Further studies investigating whether tension regulates cofilin dynamics at the wound edge will shed light on the mechanisms that balance cytoskeletal turnover and stability to drive rapid wound repair.

We demonstrate that cofilin maintains a flexible F-actin network around the wound. The flexibility of the F-actin network may facilitate filament packing as myosin motors slide the filaments past each other. Additionally, flexible actin filaments may oppose lower resistance to myosin- or crosslinker-based filament alignment[67,68], a process in which cofilin has been implicated[69] and that is associated with force generation[70-72]. Super-resolution analysis of the actin network architecture[73,74] at the wound edge will reveal whether cofilin promotes filament alignment and compaction to facilitate rapid embryonic wound healing.

An outstanding question is whether the effects of cofilin on F-actin turnover and flexibility during wound repair are related. Crosslinking increases the rigidity of F-actin networks *in vitro*[16,75] and in cells[76], and reduces turnover[76,77]. Thus, by competing with crosslinkers for actin binding[78], or by changing filament conformation[28,29] in a way that precludes crosslinking[79], cofilin could maintain a flexible F-actin network, facilitating contraction and packing. Investigating how different crosslinkers contribute to the wound healing response[80], and establishing the interplay between crosslinkers and cofilin at the wound edge, will contribute to our understanding of how the material properties of the cytoskeleton are established and regulated *in vivo*, and how they impact tissue morphogenesis.

STAR Methods

Fly stocks

Flies were maintained at room temperature and embryos were collected on apple juice agar plates kept overnight at room temperature. For live imaging, we used *sqh-GFP:utrophinABD* [39], *sqh-sqh:GFP* [41], *endo-E-cadherin:tdTomato*[81], *endo-cofilin:GFP* [34,35] and *endo-aip1:GFP* (Bloomington *Drosophila* Stock Center #50824)[36]. For LIMK overexpression, we used *UAS-LIMK* (Bloomington *Drosophila* Stock Center #9116)[82]. *UAS-LIMK* was ubiquitously driven with *daughterless-Gal4* [83].

Embryo mounting and injections

Drosophila embryos at stage 14-15 were dechorionated in 50% bleach for 2 minutes and thoroughly rinsed. Embryos were glued ventral-lateral side down to a glass coverslip using heptane glue and covered with a 1:1 mix of halocarbon oil 27 and 700 (Sigma-Aldrich). For injections, embryos were dehydrated for 8-9 minutes inside a plastic container with silica (Drierite). After dehydration, embryos were covered with the same 1:1 mix of halocarbon oil. Injections were done with a PV820 injector (World Precision Instruments) coupled to a spinning disk confocal microscope. Embryos were injected in the perivitelline space with 750 µM of Latrunculin A (Tocris Bioscience) dissolved in 50% DMSO, or with 50% DMSO as a control. Drugs are predicted to be diluted by 50-fold in the perivitelline fluid[84]. All injections were followed by a 10-minute incubation period at room temperature before imaging.

Time-lapse imaging

Embryos were imaged at room temperature using a Revolution XD spinning disk confocal microscope (Andor Technology) with a CSU-X1 confocal head and a 60X oil immersion lens (Olympus, NA 1.35). The microscope was controlled with Metamorph (Molecular Devices). Sixteen-bit Z-stacks were acquired at 0.5 µm steps every 3, 4 or 30 seconds (11 or 21 slices per stack). Maximum intensity projections were used for analysis.

Laser ablation

Laser ablations were done using a pulsed Micropoint nitrogen laser (Andor Technology) tuned to 365 nm. For wounding, 10 pulses were delivered at six spots along a 13 µm line. For spot laser ablations, 10 pulses were delivered at a single point. Samples were imaged immediately before and after ablation.

FRAP

Photobleaching experiments were done using a FRAPPA system (Andor) and a 488 nm laser. A 2.7 × 2.7 μm^2 region (10 x 10 pixels) was photobleached using a dwell time of 500 µs/pixel. Two Z-stacks were acquired 3 s apart prior to photobleaching. Photobleached regions were imaged immediately after photobleaching and every 3 s thereafter for at least 2 min.

F-actin fluctuation measurements

Living embryos expressing GFP:UtrophinABD were wounded and imaged in a spinning disk confocal microscope until wound area reached 50% of its maximum value. A single Z-slice image was collected using a 100X oil-immersion lens (NA 1.4, Olympus) to map the position of the wound edge. Disk rotation was stopped, and 1600 single Z-slice images were captured sequentially, with an exposure time of 5 ms. The pinholes that overlapped the wound edge were identified by overlaying the first image of the sequence with the image acquired before the disk was stopped.

Embryo fixation and immunofluorescent staining

Embryos at stage 14-15 were dechorionated as described above and fixed for 20 minutes in a 1:1 mix of heptane and 37% formaldehyde in phosphate buffer. Embryos were devitellinized

manually with the aid of a glass needle, stained with primary antibodies overnight at 4ºC, and incubated with secondary antibodies for 1 hour at room temperature. Primary antibodies were rabbit anti-Dm-cofilin[85] (1:500, a gift from Anna Sokac), and mouse anti-Pi-cofilin1 (1:100, sc-271921, Santa Cruz Biotechnology). Fluctuation analysis in fixed embryos was conducted in embryos stained with Phalloidin 488 (1:500, Invitrogen). Embryos were mounted in ProLong Gold (Molecular Probes) between two coverslips. Sixteen-bit Z-stacks were acquired at 0.2 µm steps (27 slices per stack). Single Z-slices were used for quantitative analysis.

Quantitative image analysis

Image analysis was done using PyJAMAS, an open-source image analysis platform that we develop[86]. To quantify the rate of wound closure and fluorescence intensities around the wound, we generated maximum intensity projections of the stacks and traced the wound edge in each frame of the time-lapse sequences using the semi-automated LiveWire tool[87], integrated in PyJAMAS. The LiveWire method uses Dijkstra's optimal path search algorithm[88] to find the brightest pixel path connecting any two pixels, and can be used to rapidly trace the wound edge[89]. We measured the rate of wound closure by fitting an exponential decay function to the curve that quantifies wound area over time and extracting the decay constant[40]. We measured the circularity, *C*, of wounds as:

$$C = 4\pi \frac{area}{perimeter^2} \qquad \text{(Eq. 1)},$$

with a perfect circle having a circularity of 1, and shapes deviating from circles having lower circularity values. Fluorescence at the wound margin was calculated as the mean pixel value under a 0.6 µm-wide mask generated by the LiveWire algorithm. Intensity values were background-subtracted using the image mode, and corrected for photobleaching by dividing by the mean image intensity at each time point. For the quantification of cofilin and Aip1 accumulation at the wound edge, a small region outside of the embryo was used for background correction calculations.

To measure retraction velocity after laser ablation, we tracked the position of the two tricellular junctions adjacent to the ablation site. Additionally, we modelled junctions as

viscoelastic elements using a Kelvin-Voigt model[44], which describes the distance *L* between the ends of the severed junction at time *t* after ablation as:

$$L(t) = D\left(1 - e^{-\frac{t}{\tau}}\right) \quad \text{(Eq. 2)},$$

where *D* is the asymptotic distance of retraction, proportional to the tension sustained by the junction, and τ is a relaxation time given by the viscosity-to-elasticity ratio.

For FRAP analysis, the fluorescence intensity in the photobleached region at time *t*, *f(t)*, was measured as:

$$f(t) = 100 \times \frac{\left(I_{ROI}(t) - I_{bg}(t)\right) - \left(I_{ROI}(0) - I_{bg}(0)\right)}{\left(I_{ROI}(before) - I_{bg}(before)\right) - \left(I_{ROI}(0) - I_{bg}(0)\right)} \times \frac{I_M(before) - I_{bg}(before)}{I_M(t) - I_{bg}(t)} \quad \text{(Eq. 3)},$$

where *t=before* is the time immediately before photobleaching, *t* = 0 is the time immediately after photobleaching, I_{ROI} is the mean pixel value within the photobleached region, I_{bg} is the background signal, calculated as the mean pixel value within a 10×10-pixel region outside the embryo, and I_M is the mean image intensity. The mobile fraction (*M*) was obtained from fitting the fluorescence recovery curve with an exponential:

$$F(t) = M\left(1 - e^{-\frac{t}{\tau_{FRAP}}}\right) \quad \text{(Eq. 4)},$$

where τ_{FRAP} is a characteristic time scale of fluorescence recovery. The half-time of fluorescence recovery, $t_{1/2}$, was calculated as[90]:

$$t_{1/2} = \log(2) \times \tau_{FRAP} \quad \text{(Eq. 5)}.$$

For F-actin fluctuation analysis, fluorescence intensities imaged through wound edge pinholes were measured using PyJAMAS. Raw intensities for each pinhole were background-subtracted using the image mode to account for camera noise. Photobleaching normalization

was conducted by dividing the fluctuation value at time *t* by the mean of all the wound edge pinhole intensities at that specific time point. Fluctuations for each pinhole trace were calculated by subtracting the temporal mean from the background-corrected and photobleaching normalized intensities. Autocorrelation results were normalized to a maximum value of 1, and were fitted to the model:

$$G(\tau) = G(0)\left(1 + \frac{\tau}{\tau_d}\right)^{-1} \quad \text{(Eq. 6)},$$

where $G(0)=1$, and τ_d is the autocorrelation decay time, related to the period of fluctuation.

Computational modelling

Contraction of the actomyosin cable at the wound edge was modelled with Cytosim[51,91], using the parameter values in Table S1. Control parameter values were adjusted in calibration experiments to approach the *in vivo* rates and dynamics of network contraction. For each condition, we simulated actin bundles made up of 8 filaments. The initial actin levels were the same in all simulations, consistent with our *in vivo* measurements (Figs. 2E-H and 3B). Thus, for instance, when we simulated scenarios with actin filament length halved, we doubled the number of bundles to preserve the same amount of actin. Similarly, actin filaments were arranged into an ellipse with dimensions typical of our *in vivo* measurements: a major axis of 50 µm and a minor axis of 20 µm, for a circularity of 0.75 (Fig. 6C). Myosin motors were assembled into myosin minifilaments of 8 motors each. Actin bundles and myosin minifilaments were distributed randomly along the ellipse in each trial, such that at the start of the simulations the actin filaments were tangential to the ellipse. Crosslinkers were distributed randomly within each bundle. Simulations were run with a time step of 0.1 seconds, evolving stochastically according to Langevin dynamics[51]. Frames showing the simulated networks at 20 second intervals were exported and analyzed using PyJAMAS.

Statistical analysis

To assess the significance of differences between two unpaired groups, we used a non-parametric Mann-Whitney test. For multigroup comparisons, we used a Kruskal-Wallis test to reject the null hypothesis, and post-hoc Dunn's tests for pairwise comparisons. To compare

parameter values over perimeter bins, we used Fisher's method for P-value combination[92]. Single comparisons were made using the Mann-Whitney test, and the obtained P-values (P_i) were combined into a joint test to determine the presence of a global effect. The Fisher method statistic (X) follows a χ^2 distribution with $\nu = 2k$ degrees of freedom, and was calculated as:

$$X = -2\sum_{i=1}^{k} \ln(P_i) \qquad \text{(Eq. 7).}$$

Declaration of interests

The authors declare no competing interests.

Acknowledgments

We are grateful to Ray Hawkins for help with image analysis. We thank Negar Balaghi, Veronica Castle, Ray Hawkins, Sasha Korolov, Willow Peterson, and Gordana Scepanovic for comments on the manuscript, and Tony Harris, Shane Hutson, and Alison McGuigan for helpful discussions. AMC was partially supported by a PhD fellowship from the Portuguese Foundation for Science and Technology (FCT). JHS was partially supported by scholarships from the Translational Biology and Engineering Program of the Ted Rogers Centre for Heart Research and the University of Toronto Excellence Award. This work was funded by grants to RFG from the Canadian Institutes of Health Research (156279 and 186188) and the Canada Foundation for Innovation (30279). RFG is the Canada Research Chair in Quantitative Cell Biology and Morphogenesis.

Table S1. Model parameters. Parameter values used in the simulations when testing the effects on network contraction of severing, filament length, filament rigidity, and filament disassembly rate. Parameters that differed across experiments are highlighted in bold.

parameter	severing	length	rigidity	disassembly	source
time step	0.1 s	0.1 s	0.1 s	0.1 s	
crosslinker length	1 µm	1 µm	1 µm	1 µm	(default)
crosslinker stiffness	100 pN/µm	100 pN/µm	100 pN/µm	100 pN/µm	(default)
actin filaments per bundle	8	8	8	8	(calibration)
crosslinkers per bundle	40	80	40	40	(calibration)
bundles per network	1000	500	1000	1000	(calibration)
# of myosin minifilaments	1600	1600	1600	1600	(calibration)
myosin minifilament rigidity	1 pN*µm^2	1 pN*µm^2	1 pN*µm^2	1 pN*µm^2	(default)
motor binding rate	5 s^{-1}	5 s^{-1}	5 s^{-1}	5 s^{-1}	(default)
motor dissociation rate	1 s^{-1}	1 s^{-1}	1 s^{-1}	1 s^{-1}	(default)
# of severing molecules	**0**	20	20	20	(calibration)
actin filament rigidity	0.01 pN*µm^2	0.01 pN*µm^2	**0.04 pN*µm^2**	0.01 pN*µm^2	[28]
actin filament length	3 µm	**6 µm**	3 µm	3 µm	[47]
actin disassembly rate	0.001 µm/s	0.001 µm/s	0.001 µm/s	**0.0005 µm/s**	(calibration)
actin assembly rate	0 µm/s	0 µm/s	0 µm/s	0 µm/s	(default)

Figure legends

Figure 1. Cofilin and its cofactor AIP1 both localize to the wound edge. (A, C) Wound closure in embryos expressing endo-cofilin:GFP (A) or endo-AIP1:GFP (C). Arrowheads indicate fluorescence accumulation at the wound edge. Red dotted lines indicate wound sites, yellow dashes outline the wounds. Time is with respect to wounding. Anterior left, ventral down. Bars, 10 µm. **(B, D)** Maximum fluorescence accumulation at the wound edge for endo-cofilin:GFP (B, $n = 4$ wounds in as many embryos) or endo-AIP1:GFP (D, $n = 7$ wounds) Error bars, SD; line, mean.

Figure 2. Cofilin is necessary for rapid wound closure. (A-B) Wound closure in control (A) and LIMK-overexpressing (B) embryos expressing GFP:UtrophinABD. Red dotted lines indicate wound sites, yellow dashes outline the wounds. Time is with respect to wounding. Anterior left, ventral down. Bars, 10 µm. **(C-H)** Wound perimeter over time (C), wound closure rate constant (D), mean or total F-actin fluorescence at the wound edge over time (E or G, respectively), or embryo averages binned by perimeter (F or H, respectively) in control (blue, $n = 10$ wounds) or LIMK-overexpressing embryos (orange, $n = 7$). (C, E, G) Error bars, standard error of the mean (SEM). (D, F, H) Error bars, SD; line, mean. * $P < 0.05$ (Mann-Whitney test).

Figure 3. Cofilin promotes F-actin turnover at the wound edge. (A) Kymographs displaying GFP:UtrophinABD FRAP in a segment of the cable at the wound edge in control (top) or LIMK-overexpressing (bottom) embryos. Red asterisks indicate the position of the wound. Yellow boxes show the photobleached region, yellow lines indicate the time of photobleaching. Anterior left, ventral down. Bars, 3 s. **(B-E)** Initial fluorescence before photobleaching (B), percent of fluorescence recovered over time (C), mobile fraction (D), and half-time of fluorescence recovery (E) for FRAP experiments in control (blue, $n = 15$ wounds) or LIMK-overexpressing embryos (orange, $n = 9$). (B, D-E) Error bars, SD; line, mean. * $P < 0.05$ (Mann-Whitney test). (C) Error bars, SEM.

Figure 4. Precise levels of F-actin turnover are necessary for rapid wound healing. (A-D) Wound closure in control (A-B) or LIMK-overexpressing embryos (C-D) injected with 50% DMSO (A, C) or 750 µM LatA (B, D), and expressing GFP:UtrophinABD. Red dotted lines indicate wound sites, yellow dashes outline the wounds. Time is with respect to wounding. Anterior left, ventral down. Bars, 10 µm. **(E-F)** Wound perimeter over time (E) and wound closure rate constant (F), for control embryos treated with

DMSO (blue, n = 8 wounds) or LatA (cyan, n = 3), and for LIMK-overexpressing embryos treated with DMSO (orange, n = 6) or with LatA (red, n = 5). (E) Error bars, SEM. (F) Error bars, SD; line, mean. * $P < 0.05$, ** $P < 0.01$ (Dunn's test).

Figure 5. Computational modelling predicts that cofilin induces F-actin severing or controls F-actin rigidity to drive rapid wound repair. (A-D) Wound closure in simulations with (A) or without (B) F-actin severing, or with flexible (C) or rigid (D) F-actin. Red represents an actin-binding protein to visualize network contraction. Time is with respect to the onset of wound healing. Bars, 10 µm. **(E-J)** Wound perimeter over time (E, H), wound closure rate constant (F, I), and simulation averages of wound circularity binned by wound perimeter (G, J) for simulations with (blue, n = 6 simulations) or without (orange, n = 10) actin severing (E-G), and with flexible (blue, n = 6) or rigid (orange, n = 6) F-actin (H-J). (E, H) Error bars, SEM. (F-G, I-J) Error bars, SD; line, mean. ** $P < 0.01$ (Fisher's method combining P-values for all 3 bins), *** $P < 0.001$ (Mann-Whitney).

Figure 6. Cofilin facilitates wound rounding. **(A-B)** Wounds at specific times during tissue repair in control (A) and LIMK-overexpressing (B) embryos. Embryos express GFP:UtrophinABD. Yellow dashes outline the wounds. Anterior left, ventral down. Bars, 10 µm. **(C-D)** Wound circularity at specific times during tissue repair (C), or for wounds of certain perimeter (D) in control (blue, n = 10 wounds) or LIMK-overexpressing embryos (orange, n = 7). Error bars, SD; line, mean. ** $P < 0.01$, *** $P < 0.005$ (Fisher's method combining P-values for all 3 bins).

Figure 7. Cofilin controls F-actin rigidity in vivo. (A) Cartoon depicting the impact of F-actin rigidity on thermal fluctuations (A) and fluorescence fluctuations in a diffraction-limited spot (A'). **(B)** F-actin cable around a wound in an embryo expressing GFP:UtrophinABD and imaged while the disk in a spinning disk confocal rotated (grayscale); and arrested disk pinholes (cyan), with sample signal collected from a pinhole (right). Anterior left, ventral down. Bars, 10 µm (left) and 1 µm (right). **(C)** Representative sample fluorescence fluctuations measured through an arrested spinning disk pinhole in a fixed embryo (cyan), or in living control (blue) and LIMK-overexpressing (orange) embryos expressing GFP:UtrophinABD. **(D-E)** Mean autocorrelation, G, (D) and autocorrelation decay times (E) for GFP:UtrophinABD fluctuations at the wound edge in control (blue, n = 19 pinholes in 13 wounds) and LIMK-overexpressing embryos (orange, n = 24 pinholes in 18 wounds). Error bars, SD; line, mean. * $P < 0.05$ (Mann-Whitney test).

Supplementary figure legends

Figure S1. LIMK overexpression inactivates cofilin in the *Drosophila* embryonic epidermis. (A-B) Control (A) and LIMK-overexpressing (B) embryos fixed and stained with antibodies against total cofilin (green in merge, middle) and P-cofilin (magenta in merge, right). Inset in A shows a contrast-stretched image of P-cofilin fluorescence in control embryos. Anterior left, ventral down. Bars, 200 µm. **(C)** P-cofilin-to-total cofilin ratio in control ($n = 3$ embryos) and LIMK-overexpressing embryos ($n = 3$). Error bars, SD; line, mean. * $P < 0.05$ (Mann-Whitney test).

Figure S2. Cofilin controls myosin turnover but not polarization during embryonic wound closure. (A-B) Wound closure in control (A) and LIMK-overexpressing (B) embryos expressing a fluorescent myosin reporter (Sqh:GFP). Yellow dashes outline the wounds. Time is with respect to wounding. Anterior left, ventral down. Bars, 10 µm. **(C-D)** Wound closure rate constant (C) and mean myosin fluorescence at the wound edge (D) in control (blue, $n = 6$ wounds) and LIMK-overexpressing embryos (orange, $n = 11$). **(E)** Kymographs displaying Sqh:GFP FRAP in a segment of the cable at the wound edge in control (top) or LIMK-overexpressing (bottom) embryos. Red asterisks indicate the position of the wound. Yellow boxes show the photobleached region, yellow lines indicate the time of photobleaching. Anterior left, ventral down. Bars, 3 s. **(F-I)** Initial fluorescence before photobleaching (F), percent of fluorescence recovered over time (G), mobile fraction (H), and half-time of fluorescence recovery (I) for FRAP experiments in control ($n = 8$ wound edge segments) and LIMK-overexpressing embryos ($n = 7$). (C, F, H-I) Error bars, SD; line, mean. * $P < 0.05$ (Mann-Whitney test). (D, G) Error bars, SEM.

Figure S3. Cofilin does not control F-actin turnover in the intact epidermis. (A) Kymographs displaying GFP:UtrophinABD FRAP in a cell-cell junction in the intact epidermis in control (top) or LIMK-overexpressing (bottom) embryos. Yellow boxes show the photobleached region, yellow lines indicate the time of photobleaching. Anterior left, ventral down. Bars, 3 s. **(B-E)** Initial fluorescence before photobleaching (B), percent of fluorescence recovered over time (C), mobile fraction (D), and half-time of fluorescence recovery (E) for FRAP experiments in control (blue, $n = 13$ junctions) or LIMK-overexpressing embryos (orange, $n = 15$). (B, D-E) Error bars, SD; line, mean. (C) Error bars, SEM.

Figure S4. Cofilin does not control tension or viscoelasticity in the *Drosophila* epidermis. (A, E) Kymographs showing laser ablation of a cell junction in the intact epidermis (A) or a segment of the wound edge (E) in control (top) or LIMK-overexpressing (bottom) embryos. Arrowheads indicate the ends of the severed structure. Red asterisks indicate the position of the wound. Yellow lines show the time of ablation. Anterior left, ventral down. Bars, 4s. **(B-D, F-H)** Retraction velocity after ablation (B, F), and Kelvin-Voigt model parameters: asymptotic distance retracted (proportional to the tension-to-elasticity ratio, C, G), and relaxation time (proportional to the viscosity-to-elasticity ratio, D, H) in control (blue, n = 19 junctions in B-D, n = 19 wounds in F-H) and LIMK-overexpressing embryos (orange, n = 14 in B-D, n = 25 in F-H). Error bars, SD; line, mean.

Figure S5. LatA treatment increases F-actin turnover. **(A)** Kymographs displaying GFP:UtrophinABD FRAP in a cell-cell junction in the epidermis of embryos treated with 50% DMSO (blue) or 750 µM LatA (cyan). Yellow boxes show the photobleached region, yellow lines indicate the time of photobleaching. Anterior left, ventral down. Bars, 3 s. **(B-E)** Initial fluorescence before photobleaching (B), percent of fluorescence recovered over time (C), mobile fraction (D), and half-time of fluorescence recovery (E) for FRAP experiments in DMSO-treated (blue, n = 9 junctions) or LatA-treated (cyan, n = 10 junctions) embryos. (B, D-E) Error bars, SD; line, mean. * $P < 0.05$ (Mann-Whitney test). (C) Error bars, SEM.

Figure S6. Computational modelling predicts that changes in filament length and filament disassembly rates do not recapitulate the effects of cofilin on wound closure. (A-D) Wound closure in simulations with short (A) or long (B) actin filaments, or with faster (C) or slower (D) F-actin disassembly. Red represents an actin-binding protein to visualize network contraction. Time is with respect to the onset of wound healing. Bars, 10 µm. **(E-J)** Wound perimeter over time (E, H), wound closure rate constant (F, I), and simulation averages of wound circularity binned by wound perimeter (G, J) for simulations with short (blue, n = 6 simulations) or long (orange, n = 6) actin filaments (E-G), and with faster (blue, n = 6) or slower (orange, n = 6) F-actin disassembly (H-J). (E, H) Error bars, SEM. (F-G, I-J) Error bars, SD; line, mean. *** $P < 0.001$ (Mann-Whitney).

Figure S7. F-actin turnover facilitates wound rounding. **(A-D)** Wound closure at different wound perimeters in control (A-B) and LIMK-overexpressing (C-D) embryos treated with 50% DMSO (A, C) or 750 µM LatA (B, D). Embryos expressed GFP:UtrophinABD. Yellow dashes outline the wounds. Anterior left, ventral down. Bars, 10 µm. **(E)** Circularity for wounds of a certain perimeter in control embryos treated with DMSO (blue, n = 8 wounds) or LatA (cyan, n = 3), and in LIMK-overexpressing embryos treated with

DMSO (orange, $n = 6$) or with LatA (red, $n = 5$). Error bars, SD; line, mean. * $P < 0.05$, ** $P < 0.01$, *** $P < 0.001$ (Dunn's test).

Supplementary video legends

Video S1. Cofilin is necessary for rapid wound closure. Wound closure in control (left) and LIMK-overexpressing (right) embryos expressing GFP:UtrophinABD. Images were acquired every 30 s. Time after wounding is shown. Anterior left, ventral down.

Video S2. Precise levels of F-actin turnover are necessary for rapid wound healing. Wound closure in control (first and second from the left) or LIMK-overexpressing embryos (third and fourth) injected with 50% DMSO (first and third) or 750 µm of LatA (second and fourth). Images were acquired every 30 s. Time after wounding is shown. Anterior left, ventral down.

Video S3. Computational modelling predicts that cofilin may induce F-actin severing to drive rapid wound repair. Wound closure in simulations with (left) or without (right) F-actin severing. Red represents an actin-binding protein to visualize network contraction. Images were exported every 20 s. Time is with respect to the onset of wound healing.

Video S4. Computational modelling predicts that cofilin may control F-actin rigidity to drive rapid wound repair. Wound closure in simulations with flexible (left) or rigid (right) F-actin. Red represents an actin-binding protein to visualize network contraction. Images were exported every 20 s. Time is with respect to the onset of wound healing.

References

1. Rowlatt, U. (1979). Intrauterine wound healing in a 20 week human fetus. Virchows Archiv A Pathological Anatomy and Histology *381*, 353-361. 10.1007/bf00432477.
2. Longaker, M.T., Whitby, D.J., Adzick, N.S., Crombleholme, T.M., Langer, J.C., Duncan, B.W., Bradley, S.M., Stern, R., Ferguson, M.W., and Harrison, M.R. (1990). Studies in fetal wound healing, VI. Second and early third trimester fetal wounds demonstrate rapid collagen deposition without scar formation. Journal of Pediatric Surgery *25*, 63-68; discussion 68-69. 10.1016/s0022-3468(05)80165-4.
3. Martin, P., and Lewis, J. (1992). Actin cables and epidermal movement in embryonic wound healing. Nature *360*, 179-183. 10.1038/360179a0.
4. McCluskey, J., Hopkinson-Woolley, J., Luke, B., and Martin, P. (1993). A study of wound healing in the E11.5 mouse embryo by light and electron microscopy. Tissue Cell *25*, 173-181. 10.1016/0040-8166(93)90017-f.
5. Kiehart, D.P., Galbraith, C.G., Edwards, K.A., Rickoll, W.L., and Montague, R.A. (2000). Multiple Forces Contribute to Cell Sheet Morphogenesis for Dorsal Closure in Drosophila. Journal of Cell Biology *149*, 471-490. 10.1083/jcb.149.2.471.
6. Wood, W., Jacinto, A., Grose, R., Woolner, S., Gale, J., Wilson, C., and Martin, P. (2002). Wound healing recapitulates morphogenesis in Drosophila embryos. Nature Cell Biology *4*, 907-912. 10.1038/ncb875.
7. Abreu-Blanco, M.T., Verboon, J.M., Liu, R., Watts, J.J., and Parkhurst`divisionparkhurst, S.M. (2012). Drosophila embryos close epithelial wounds using a combination of cellular protrusions and an actomyosin purse string. Journal of Cell Science *125*, 5984-5997. 10.1242/jcs.109066.
8. Fernandez-Gonzalez, R., and Zallen, J.A. (2013). Wounded cells drive rapid epidermal repair in the early Drosophila embryo. Molecular Biology of the Cell *24*, 3227-3237. 10.1091/mbc.e13-05-0228.
9. Kobb, A.B., Zulueta-Coarasa, T., and Fernandez-Gonzalez, R. (2017). Tension regulates myosin dynamics during Drosophila embryonic wound repair. Journal of Cell Science *130*, 689-696. 10.1242/jcs.196139.
10. Zulueta-Coarasa, T., and Fernandez-Gonzalez, R. (2018). Dynamic force patterns promote collective cell movements during embryonic wound repair. Nature Physics *14*, 750-758. 10.1038/s41567-018-0111-2.
11. Murrell, M., Oakes, P.W., Lenz, M., and Gardel, M.L. (2015). Forcing cells into shape: the mechanics of actomyosin contractility. Nature Reviews Molecular Cell Biology *16*, 486-498.
12. Koenderink, G.H., and Paluch, E.K. (2018). Architecture shapes contractility in actomyosin networks. Current Opinion in Cell Biology *50*, 79-85.
13. Murrell, M.P., and Gardel, M.L. (2012). F-actin buckling coordinates contractility and severing in a biomimetic actomyosin cortex. Proceedings of the National Academy of Sciences *109*, 20820-20825.
14. Kasza, K., Broedersz, C., Koenderink, G., Lin, Y., Messner, W., Millman, E., Nakamura, F., Stossel, T., MacKintosh, F., and Weitz, D. (2010). Actin filament length tunes elasticity of flexibly cross-linked actin networks. Biophysical Journal *99*, 1091-1100.
15. Sato, M., Schwarz, W.H., and Pollard, T.D. (1987). Dependence of the mechanical properties of actin/α-actinin gels on deformation rate. Nature *325*, 828-830.

16. Gardel, M.L., Shin, J.H., MacKintosh, F., Mahadevan, L., Matsudaira, P., and Weitz, D.A. (2004). Elastic behavior of cross-linked and bundled actin networks. Science *304*, 1301-1305.
17. Bendix, P.M., Koenderink, G.H., Cuvelier, D., Dogic, Z., Koeleman, B.N., Brieher, W.M., Field, C.M., Mahadevan, L., and Weitz, D.A. (2008). A quantitative analysis of contractility in active cytoskeletal protein networks. Biophysical Journal *94*, 3126-3136.
18. Ennomani, H., Letort, G., Guérin, C., Martiel, J.L., Cao, W., Nédélec, F., De La Cruz, E.M., Théry, M., and Blanchoin, L. (2016). Architecture and Connectivity Govern Actin Network Contractility. Current Biology *26*, 616-626. 10.1016/j.cub.2015.12.069.
19. Akenuwa, O.H., and Abel, S.M. (2023). Organization and dynamics of cross-linked actin filaments in confined environments. Biophysical Journal *122*, 30-42.
20. Costa, K.D., Hucker, W.J., and Yin, F.C.P. (2002). Buckling of actin stress fibers: a new wrinkle in the cytoskeletal tapestry. Cell Motility and the Cytoskeleton *52*, 266-274.
21. Mendes Pinto, I., Rubinstein, B., Kucharavy, A., Unruh, J.R., and Li, R. (2012). Actin Depolymerization Drives Actomyosin Ring Contraction during Budding Yeast Cytokinesis. Developmental Cell *22*, 1247-1260. 10.1016/j.devcel.2012.04.015.
22. Xue, Z., and Sokac, A.M. (2016). Back-to-back mechanisms drive actomyosin ring closure during Drosophila embryo cleavage. Journal of Cell Biology *215*, 335-344. 10.1083/jcb.201608025.
23. Jodoin, J.N., Coravos, J.S., Chanet, S., Vasquez, C.G., Tworoger, M., Kingston, E.R., Perkins, L.A., Perrimon, N., and Martin, A.C. (2015). Stable Force Balance between Epithelial Cells Arises from F-Actin Turnover. Developmental Cell *35*, 685-697. 10.1016/j.devcel.2015.11.018.
24. Antunes, M., Pereira, T., Cordeiro, J.V., Almeida, L., and Jacinto, A. (2013). Coordinated waves of actomyosin flow and apical cell constriction immediately after wounding. Journal of Cell Biology *202*, 365-379. 10.1083/jcb.201211039.
25. Kobb, A.B., Rothenberg, K.E., and Fernandez-Gonzalez, R. (2019). Actin and myosin dynamics are independent during Drosophila embryonic wound repair. Molecular Biology of the Cell *30*, 2901-2912. 10.1091/mbc.E18-11-0703.
26. Bamburg, J.R., and Bernstein, B.W. (2010). Roles of ADF/cofilin in actin polymerization and beyond. F1000 Biology Reports *2*, 62-62. 10.3410/B2-62.
27. Carlier, M.F., Laurent, V., Santolini, J., Melki, R., Didry, D., Xia, G.X., Hong, Y., Chua, N.H., and Pantaloni, D. (1997). Actin depolymerizing factor (ADF/cofilin) enhances the rate of filament turnover: implication in actin-based motility. The Journal of Cell Biology *136*, 1307-1322. 10.1083/JCB.136.6.1307.
28. McCullough, B.R., Blanchoin, L., Martiel, J.-L., and De La Cruz, E.M. (2008). Cofilin Increases the Bending Flexibility of Actin Filaments: Implications for Severing and Cell Mechanics. Journal of Molecular Biology *381*, 550-558. 10.1016/j.jmb.2008.05.055.
29. Brannon, Elena, Christine, Kang, H., Alan, Henn, A., Cao, W., Suarez, C., Martiel, J.-L., Blanchoin, L., et al. (2011). Cofilin-Linked Changes in Actin Filament Flexibility Promote Severing. Biophysical Journal *101*, 151-159. 10.1016/j.bpj.2011.05.049.
30. Prochniewicz, E., Janson, N., Thomas, D.D., and De la Cruz, E.M. (2005). Cofilin increases the torsional flexibility and dynamics of actin filaments. J Mol Biol *353*, 990-1000. 10.1016/j.jmb.2005.09.021.
31. Elam, W.A., Kang, H., and De La Cruz, E.M. (2013). Biophysics of actin filament severing by cofilin. FEBS Letters *587*, 1215-1219. 10.1016/j.febslet.2013.01.062.

32. Agnew, B.J., Minamide, L.S., and Bamburg, J.R. (1995). Reactivation of Phosphorylated Actin Depolymerizing Factor and Identification of the Regulatory Site. Journal of Biological Chemistry *270*, 17582-17587. 10.1074/jbc.270.29.17582.
33. Arber, S., Barbayannis, F.A., Hanser, H., Schneider, C., Stanyon, C.A., Bernard, O., and Caroni, P. (1998). Regulation of actin dynamics through phosphorylation of cofilin by LIM-kinase. Nature *393*, 805-809. 10.1038/31729.
34. Morin, X., Daneman, R., Zavortink, M., and Chia, W. (2001). A protein trap strategy to detect GFP-tagged proteins expressed from their endogenous loci in Drosophila. Proc Natl Acad Sci U S A *98*, 15050-15055. 10.1073/pnas.261408198.
35. Ikawa, K., and Sugimura, K. (2018). AIP1 and cofilin ensure a resistance to tissue tension and promote directional cell rearrangement. Nature Communications *9*. 10.1038/s41467-018-05605-7.
36. Morin, X., Daneman, R., Zavortink, M., and Chia, W. (2001). A protein trap strategy to detect GFP-tagged proteins expressed from their endogenous loci in Drosophila. Proceedings of the National Academy of Sciences *98*, 15050-15055.
37. Brand, A.H., and Perrimon, N. (1993). Targeted gene expression as a means of altering cell fates and generating dominant phenotypes. Development *118*, 401.
38. Perrin, L., Bloyer, S., Ferraz, C., Agrawal, N., Sinha, P., and Dura, J.M. (2003). The Leucine Zipper Motif of the Drosophila AF10 Homologue Can Inhibit PRE-Mediated Repression: Implications for Leukemogenic Activity of Human MLL-AF10 Fusions. Molecular and Cellular Biology *23*, 119-130. 10.1128/MCB.23.1.119-130.2003.
39. Rauzi, M., Lenne, P.-F., and Lecuit, T. (2010). Planar polarized actomyosin contractile flows control epithelial junction remodelling. Nature *468*, 1110-1114. 10.1038/nature09566.
40. Hunter, M.V., Willoughby, P.M., Bruce, A.E., and Fernandez-Gonzalez, R. (2018). Oxidative stress orchestrates cell polarity to promote embryonic wound healing. Developmental Cell *47*, 377-387. e374.
41. Royou, A., Field, C., Sisson, J.C., Sullivan, W., and Karess, R. (2003). Reassessing the Role and Dynamics of Nonmuscle Myosin II during Furrow Formation in Early Drosophila Embryos. Molecular Biology of the Cell *15*, 838-850. 10.1091/mbc.e03-06-0440.
42. Tetley, R.J., Staddon, M.F., Heller, D., Hoppe, A., Banerjee, S., and Mao, Y. (2019). Tissue Fluidity Promotes Epithelial Wound Healing. Nat Phys *15*, 1195-1203. 10.1038/s41567-019-0618-1.
43. Hutson, M.S., Tokutake, Y., Chang, M.S., Bloor, J.W., Venakides, S., Kiehart, D.P., and Edwards, G.S. (2003). Forces for morphogenesis investigated with laser microsurgery and quantitative modeling. Science *300*, 145-149. 10.1126/science.1079552.
44. Zulueta-Coarasa, T., and Fernandez-Gonzalez, R. (2015). Laser ablation to investigate cell and tissue mechanics in vivo. In Integrative Mechanobiology: Micro- and Nano-Techniques in Cell Mechanobiology, Y. Sun, D. Kim, and C. Simmons, eds. (Cambridge University Press), pp. 128-147. doi:10.1017/CBO9781139939751.009.
45. Fujiwara, I., Zweifel, M.E., Courtemanche, N., and Pollard, T.D. (2018). Latrunculin A Accelerates Actin Filament Depolymerization in Addition to Sequestering Actin Monomers. Current Biology *28*, 3183-3192.e3182. 10.1016/j.cub.2018.07.082.
46. Kremneva, E., Makkonen, M.H., Skwarek-Maruszewska, A., Gateva, G., Michelot, A., Dominguez, R., and Lappalainen, P. (2014). Cofilin-2 controls actin filament length in muscle sarcomeres. Dev Cell *31*, 215-226. 10.1016/j.devcel.2014.09.002.

47. Robaszkiewicz, K., Śliwinska, M., and Moraczewska, J. (2020). Regulation of Actin Filament Length by Muscle Isoforms of Tropomyosin and Cofilin. International Journal of Molecular Sciences *21*, 4285. 10.3390/ijms21124285.
48. Jermyn, A.S., Cao, W., Elam, W.A., De La Cruz, E.M., and Lin, M.M. (2020). Directional allosteric regulation of protein filament length. Physical Review E *101*, 032409. 10.1103/PhysRevE.101.032409.
49. Wioland, H., Guichard, B., Senju, Y., Myram, S., Lappalainen, P., Egou, A.J., and Romet-Lemonne, G. (2017). ADF/Cofilin Accelerates Actin Dynamics by Severing Filaments and Promoting Their Depolymerization at Both Ends. Current Biology *27*. 10.1016/j.cub.2017.05.048.
50. Pavlov, D., Muhlrad, A., Cooper, J., Wear, M., and Reisler, E. (2007). Actin filament severing by cofilin. Journal of Molecular Biology *365*, 1350-1358. 10.1016/j.jmb.2006.10.102.
51. Nedelec, F., and Foethke, D. (2007). Collective Langevin dynamics of flexible cytoskeletal fibers. New Journal of Physics *9*, 427.
52. Bohdan, M., Sprakel, J., and van der Gucht, J. (2016). Multiple relaxation modes in associative polymer networks with varying connectivity. Physical Review E *94*, 032507. 10.1103/PhysRevE.94.032507.
53. Zhang, E., Zhao, Y., Yang, W., Chen, H., Liu, W., Dai, X., Qiu, X., and Ji, X. (2017). Viscoelastic behaviour and relaxation modes of one polyamic acid organogel studied by rheometers and dynamic light scattering. Soft Matter *14*, 73-82. 10.1039/c7sm02185b.
54. Sun, Z.G., Yadav, V., Amiri, S., Cao, W., Enrique, M., and Murrell, M. (2024). Cofilin-mediated actin filament network flexibility facilitates 2D to 3D actomyosin shape change. European Journal of Cell Biology *103*, 151379.
55. Sisan, D.R., Arevalo, R., Graves, C., McAllister, R., and Urbach, J.S. (2006). Spatially resolved fluorescence correlation spectroscopy using a spinning disk confocal microscope. Biophysical journal *91*, 4241-4252.
56. Needleman, D.J., Xu, Y., and Mitchison, T.J. (2009). Pin-hole array correlation imaging: highly parallel fluorescence correlation spectroscopy. Biophysical Journal *96*, 5050-5059.
57. Hunter, M.V., Lee, D.M., Harris, T.J.C., and Fernandez-Gonzalez, R. (2015). Polarized E-cadherin endocytosis directs actomyosin remodeling during embryonic wound repair. J Cell Biol *210*, 801-816. 10.1083/JCB.201501076.
58. Razzell, W., Bustillo, M.E., and Zallen, J.A. (2018). The force-sensitive protein Ajuba regulates cell adhesion during epithelial morphogenesis. The Journal of Cell Biology *217*, 3715-3730. 10.1083/jcb.201801171.
59. Rothenberg, K.E., Chen, Y., McDonald, J.A., and Fernandez-Gonzalez, R. (2023). Rap1 coordinates cell-cell adhesion and cytoskeletal reorganization to drive collective cell migration in vivo. Current Biology *33*, 2587-2601. e2585.
60. Bamburg, J.R. (1999). Proteins of the ADF/cofilin family: essential regulators of actin dynamics. Annual Review of Cell and Developmental Biology *15*, 185-230.
61. Niwa, R., Nagata-Ohashi, K., Takeichi, M., Mizuno, K., and Uemura, T. (2002). Control of Actin Reorganization by Slingshot, a Family of Phosphatases that Dephosphorylate ADF/Cofilin. Cell *108*, 233-246. 10.1016/s0092-8674(01)00638-9.
62. Wang, Y., Shibasaki, F., and Mizuno, K. (2005). Calcium signal-induced cofilin dephosphorylation is mediated by Slingshot via calcineurin. Journal of Biological Chemistry *280*, 12683-12689.

63. Kim, J.-S., Huang, T.Y., and Bokoch, G.M. (2009). Reactive oxygen species regulate a slingshot-cofilin activation pathway. Molecular Biology of the Cell *20*, 2650-2660.
64. Fernandez-Gonzalez, R., Simoes, S.d.M., Röper, J.-C., Eaton, S., and Zallen, J.A. (2009). Myosin II Dynamics Are Regulated by Tension in Intercalating Cells. Developmental Cell *17*, 736-743. 10.1016/j.devcel.2009.09.003.
65. Kovács, M., Thirumurugan, K., Knight, P.J., and Sellers, J.R. (2007). Load-dependent mechanism of nonmuscle myosin 2. Proceedings of the National Academy of Sciences *104*, 9994-9999.
66. Hayakawa, K., Tatsumi, H., and Sokabe, M. (2011). Actin filaments function as a tension sensor by tension-dependent binding of cofilin to the filament. Journal of Cell Biology *195*, 721-727. 10.1083/jcb.201102039.
67. Lieleg, O., Claessens, M.M., Heussinger, C., Frey, E., and Bausch, A.R. (2007). Mechanics of bundled semiflexible polymer networks. Physical Review Letters *99*, 088102.
68. Butt, T., Mufti, T., Humayun, A., Rosenthal, P.B., Khan, S., Khan, S., and Molloy, J.E. (2010). Myosin motors drive long range alignment of actin filaments 2. Journal of Biological Chemistry *285*, 4964-4974.
69. Mseka, T., Bamburg, J.R., and Cramer, L.P. (2007). ADF/cofilin family proteins control formation of oriented actin-filament bundles in the cell body to trigger fibroblast polarization. Journal of Cell Science *120*, 4332-4344.
70. Bidone, T.C., Tang, H., and Vavylonis, D. (2014). Dynamic network morphology and tension buildup in a 3D model of cytokinetic ring assembly. Biophysical Journal *107*, 2618-2628.
71. Stachowiak, M.R., Laplante, C., Chin, H.F., Guirao, B., Karatekin, E., Pollard, T.D., and O'Shaughnessy, B. (2014). Mechanism of cytokinetic contractile ring constriction in fission yeast. Developmental Cell *29*, 547-561.
72. Spira, F., Cuylen-Haering, S., Mehta, S., Samwer, M., Reversat, A., Verma, A., Oldenbourg, R., Sixt, M., and Gerlich, D.W. (2017). Cytokinesis in vertebrate cells initiates by contraction of an equatorial actomyosin network composed of randomly oriented filaments. eLife *6*, e30867.
73. Garlick, E., Faulkner, E.L., Briddon, S.J., and Thomas, S.G. (2022). Simple methods for quantifying super-resolved cortical actin. Scientific Reports *12*, 2715.
74. Hui, J., Nakamura, M., Dubrulle, J., and Parkhurst, S.M. (2023). Coordinated efforts of different actin filament populations are needed for optimal cell wound repair. Molecular Biology of the Cell *34*, ar15. 10.1091/mbc.E22-05-0155.
75. Schmoller, K., Lieleg, O., and Bausch, A. (2009). Structural and viscoelastic properties of actin/filamin networks: cross-linked versus bundled networks. Biophysical Journal *97*, 83-89.
76. Katsuta, H., Okuda, S., Nagayama, K., Machiyama, H., Kidoaki, S., Kato, M., Sokabe, M., Miyata, T., and Hirata, H. (2023). Actin crosslinking by α-actinin averts viscous dissipation of myosin force transmission in stress fibers. IScience *26*.
77. Tilney, L.G., Connelly, P.S., Ruggiero, L., Vranich, K.A., and Guild, G.M. (2003). Actin filament turnover regulated by cross-linking accounts for the size, shape, location, and number of actin bundles in Drosophila bristles. Molecular Biology of the Cell *14*, 3953-3966.

78. Breitsprecher, D., Koestler, S.A., Chizhov, I., Nemethova, M., Mueller, J., Goode, B.L., Small, J.V., Rottner, K., and Faix, J. (2011). Cofilin cooperates with fascin to disassemble filopodial actin filaments. Journal of Cell Science *124*, 3305-3318.
79. Hylton, R.K., Heebner, J.E., Grillo, M.A., and Swulius, M.T. (2022). Cofilactin filaments regulate filopodial structure and dynamics in neuronal growth cones. Nature Communications *13*, 2439.
80. Lehne, F., and Bogdan, S. (2023). Getting cells into shape by calcium-dependent actin cross-linking proteins. Frontiers in Cell and Developmental Biology *11*, 1171930.
81. Huang, J., Zhou, W., Dong, W., Watson, A.M., and Hong, Y. (2009). Directed, efficient, and versatile modifications of the *Drosophila* genome by genomic engineering. Proceedings of the National Academy of Sciences *106*, 8284-8289. doi:10.1073/pnas.0900641106.
82. Ng, J., and Luo, L. (2004). Rho GTPases Regulate Axon Growth through Convergent and Divergent Signaling Pathways. Neuron *44*, 779-793. 10.1016/j.neuron.2004.11.014.
83. Wodarz, A., Hinz, U., Engelbert, M., and Knust, E. (1995). Expression of crumbs confers apical character on plasma membrane domains of ectodermal epithelia of drosophila. Cell *82*, 67-76. 10.1016/0092-8674(95)90053-5.
84. Foe, V.E., and Alberts, B.M. (1983). Studies of nuclear and cytoplasmic behaviour during the five mitotic cycles that precede gastrulation in Drosophila embryogenesis. Journal of Cell Science *61*, 31-70.
85. Figard, L., Zheng, L., Biel, N., Coleman, S., Golding, I., Marie, A., and Correspondence, S. (2019). Cofilin-Mediated Actin Stress Response Is Maladaptive in Heat-Stressed Embryos. Cell Reports *26*, 3493-3501.e3494. 10.1016/j.celrep.2019.02.092.
86. Fernandez-Gonzalez, R., Balaghi, N., Wang, K., Hawkins, R., Rothenberg, K., McFaul, C., Schimmer, C., Ly, M., do Carmo, A.M., Scepanovic, G., et al. (2022). PyJAMAS: open-source, multimodal segmentation and analysis of microscopy images. Bioinformatics *38*, 594-596. 10.1093/bioinformatics/btab589.
87. Fernandez-Gonzalez, R., and Zallen, J.A. (2011). Oscillatory behaviors and hierarchical assembly of contractile structures in intercalating cells. Physical Biology *8*, 045005. 10.1088/1478-3975/8/4/045005.
88. Dijkstra, E.W. (1959). A note on two problems in connexion with graphs. Numerische Mathematik *1*, 269-271. 10.1007/bf01386390.
89. Scepanovic, G., Florea, A., and Fernandez-Gonzalez, R. (2021). Multiscale In Vivo Imaging of Collective Cell Migration in Drosophila Embryos. In Methods Mol Biol., (Springer US), pp. 199-224. 10.1007/978-1-0716-0779-4_17.
90. Pines, M., Das, R., Ellis, S.J., Morin, A., Czerniecki, S., Yuan, L., Klose, M., Coombs, D., and Tanentzapf, G. (2012). Mechanical force regulates integrin turnover in Drosophila in vivo. Nature Cell Biology *14*, 935-943.
91. Lugo, C.A., Saikia, E., and Nedelec, F. (2023). A typical workflow to simulate cytoskeletal systems. JoVE (Journal of Visualized Experiments), e64125.
92. Fisher, R.A. (1932). Statistical methods for research workers. In Breakthroughs in statistics: Methodology and distribution, (Springer), pp. 66-70.

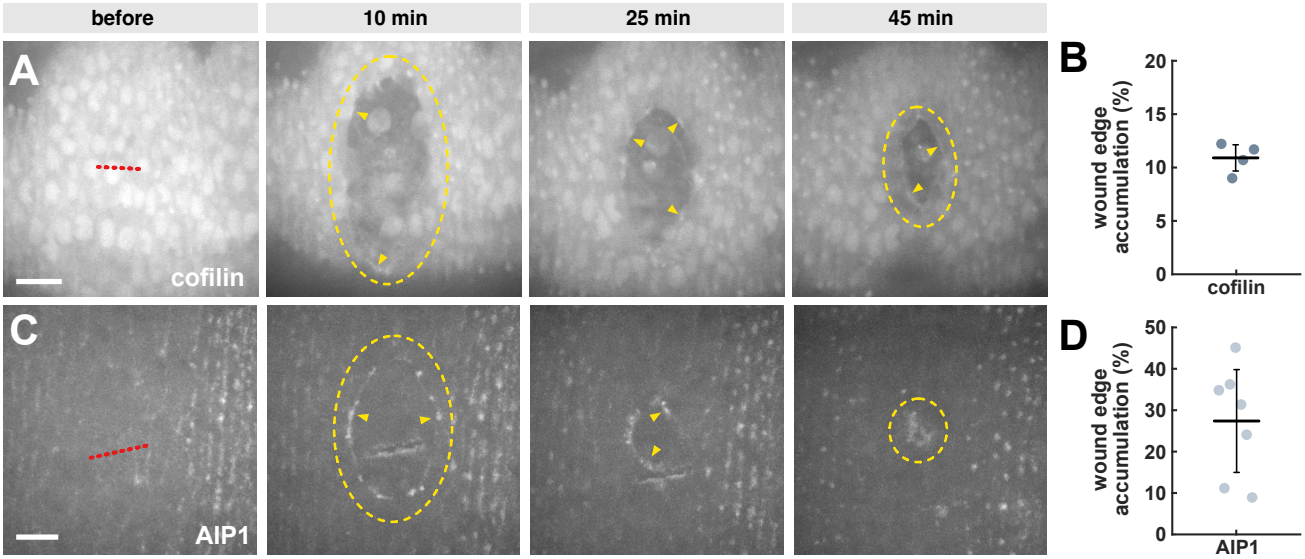

Figure 1. Cofilin and its cofactor AIP1 both localize to the wound edge. (A, C) Wound closure in embryos expressing endo-cofilin:GFP (A) or endo-AIP1:GFP (C). Arrowheads indicate fluorescence accumulation at the wound edge. Red dotted lines indicate wound sites, yellow dashes outline the wounds. Time is with respect to wounding. Anterior left, ventral down. Bars, 10 µm. **(B, D)** Maximum fluorescence accumulation at the wound edge for endo-cofilin:GFP (B, n = 4 wounds in as many embryos) or endo-AIP1:GFP (D, n = 7 wounds) Error bars, SD; line, mean.

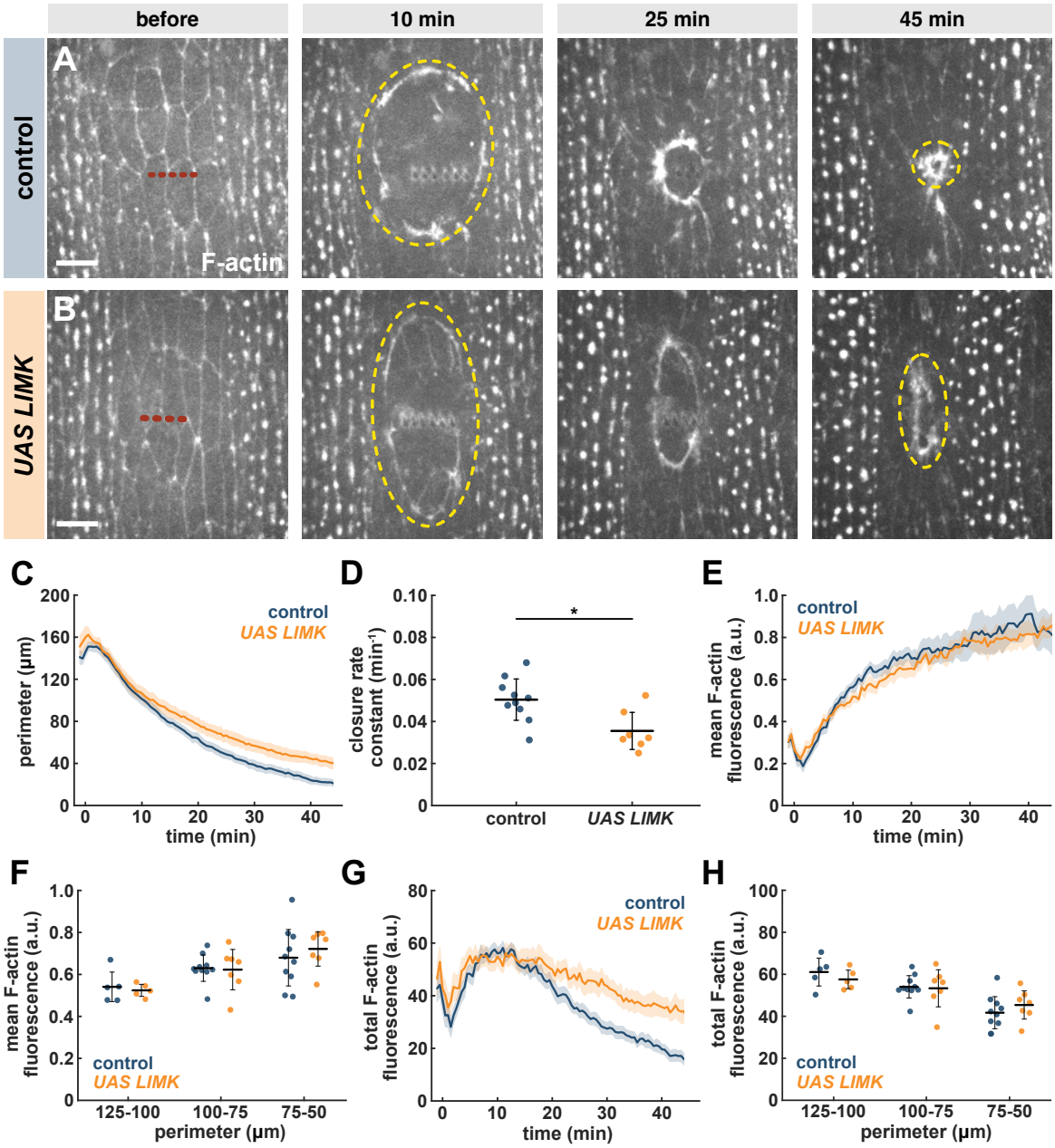

Figure 2. Cofilin is necessary for rapid wound closure. (A-B) Wound closure in control (A) and LIMK-overexpressing (B) embryos expressing GFP:UtrophinABD. Red dotted lines indicate wound sites, yellow dashes outline the wounds. Time is with respect to wounding. Anterior left, ventral down. Bars, 10 µm. **(C-H)** Wound perimeter over time (C), wound closure rate constant (D), mean or total F-actin fluorescence at the wound edge over time (E or G, respectively), or embryo averages binned by perimeter (F or H, respectively) in control (blue, $n = 10$ wounds) or LIMK-overexpressing embryos (orange, $n = 7$). (C, E, G) Error bars, standard error of the mean (SEM). (D, F, H) Error bars, SD; line, mean. * $P < 0.05$ (Mann-Whitney test).

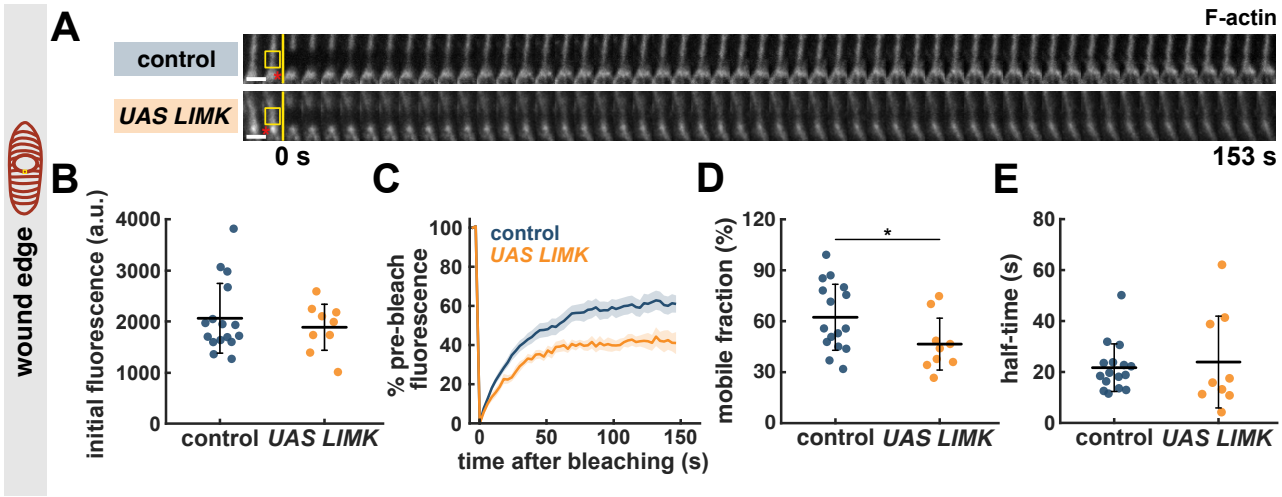

Figure 3. Cofilin promotes F-actin turnover at the wound edge. (A) Kymographs displaying GFP:UtrophinABD FRAP in a segment of the cable at the wound edge in control (top) or LIMK-overexpressing (bottom) embryos. Red asterisks indicate the position of the wound. Yellow boxes show the photobleached region, yellow lines indicate the time of photobleaching. Anterior left, ventral down. Bars, 3 s. **(B-E)** Initial fluorescence before photobleaching (B), percent of fluorescence recovered over time (C), mobile fraction (D), and half-time of fluorescence recovery (E) for FRAP experiments in control (blue, n = 15 wounds) or LIMK-overexpressing embryos (orange, n = 9). (B, D-E) Error bars, SD; line, mean. * $P < 0.05$ (Mann-Whitney test). (C) Error bars, SEM.

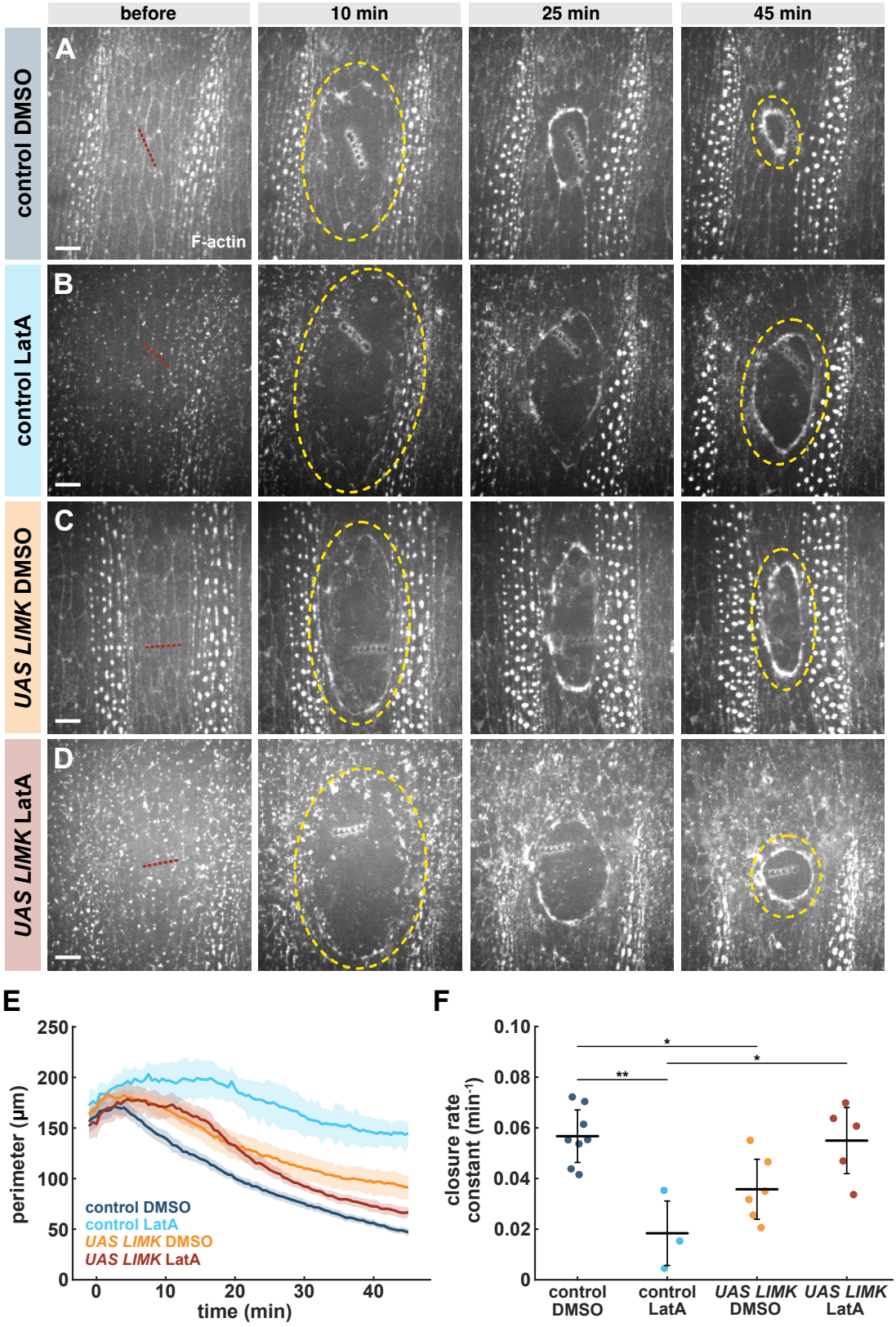

Figure 4. Precise levels of F-actin turnover are necessary for rapid wound healing. (A-D) Wound closure in control (A-B) or LIMK-overexpressing embryos (C-D) injected with 50% DMSO

(A, C) or 750 µM LatA (B, D), and expressing GFP:UtrophinABD. Red dotted lines indicate wound sites, yellow dashes outline the wounds. Time is with respect to wounding. Anterior left, ventral down. Bars, 10 µm. **(E-F)** Wound perimeter over time (E) and wound closure rate constant (F), for control embryos treated with DMSO (blue, $n = 8$ wounds) or LatA (cyan, $n = 3$), and for LIMK-overexpressing embryos treated with DMSO (orange, $n = 6$) or with LatA (red, $n = 5$). (E) Error bars, SEM. (F) Error bars, SD; line, mean. * $P < 0.05$, ** $P < 0.01$ (Dunn's test).

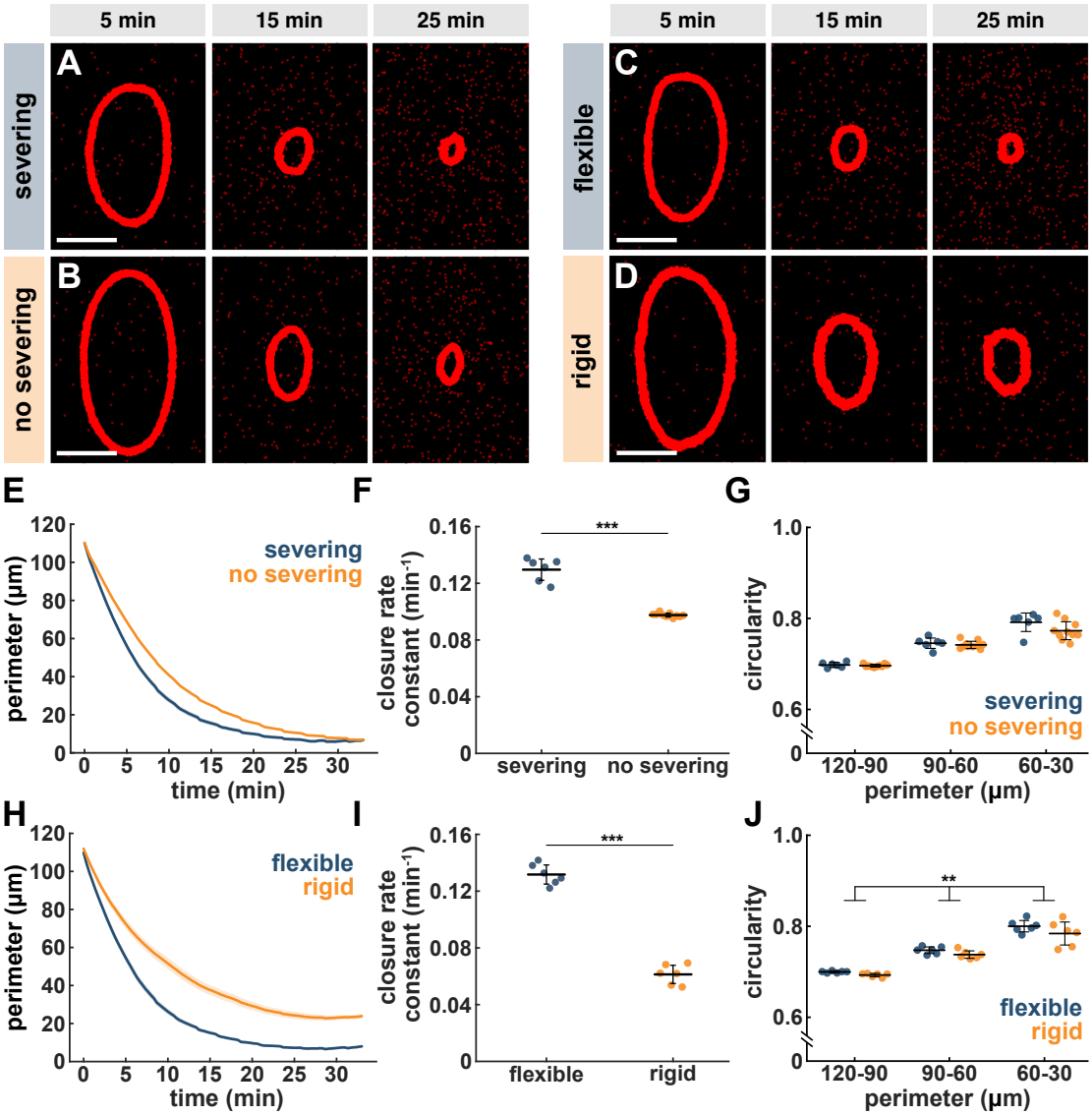

Figure 5. Computational modelling predicts that cofilin induces F-actin severing or controls F-actin rigidity to drive rapid wound repair. (A-D) Wound closure in simulations with (A) or without (B) F-actin severing, or with flexible (C) or rigid (D) F-actin. Red represents an actin-binding protein to visualize network contraction. Time is with respect to the onset of wound healing. Bars, 10 µm. **(E-J)** Wound perimeter over time (E, H), wound closure rate constant (F, I), and simulation averages of wound circularity binned by wound perimeter (G, J) for simulations with (blue, n = 6 simulations) or without (orange, n = 10) actin severing (E-G), and with flexible (blue, n = 6) or rigid (orange, n = 6) F-actin (H-J). (E, H) Error bars, SEM. (F-G, I-J) Error bars, SD; line, mean. ** $P < 0.01$ (Fisher's method combining P-values for all 3 bins), *** $P < 0.001$ (Mann-Whitney).

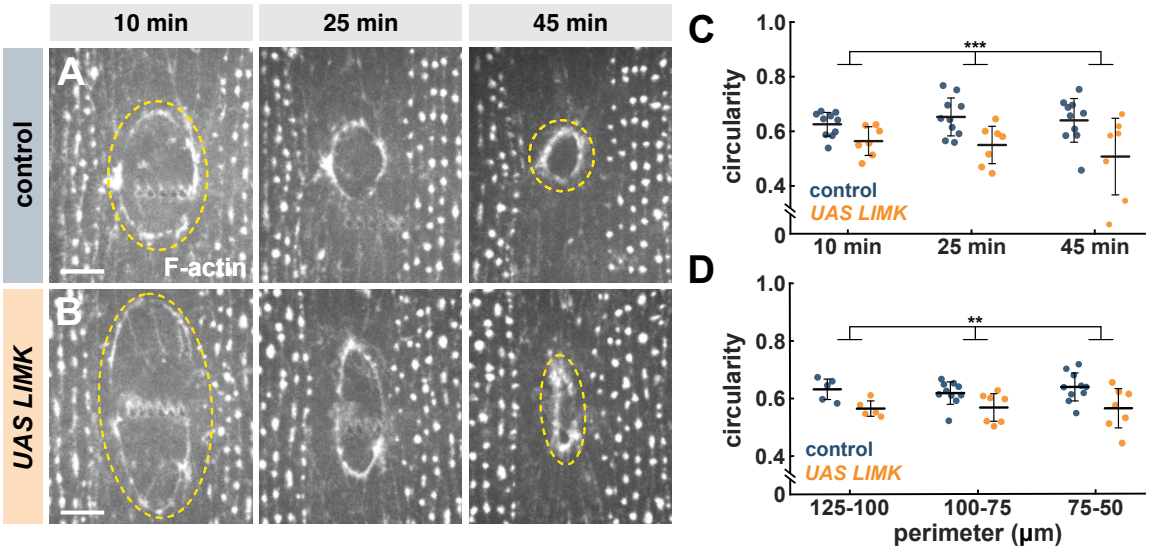

Figure 6. Cofilin facilitates wound rounding. **(A-B)** Wounds at specific times during tissue repair in control (A) and LIMK-overexpressing (B) embryos. Embryos express GFP:UtrophinABD. Yellow dashes outline the wounds. Anterior left, ventral down. Bars, 10 μm. **(C-D)** Wound circularity at specific times during tissue repair (C), or for wounds of certain perimeter (D) in control (blue, n = 10 wounds) or LIMK-overexpressing embryos (orange, n = 7). Error bars, SD; line, mean. ** $P < 0.01$, *** $P < 0.005$ (Fisher's method combining P-values for all 3 bins).

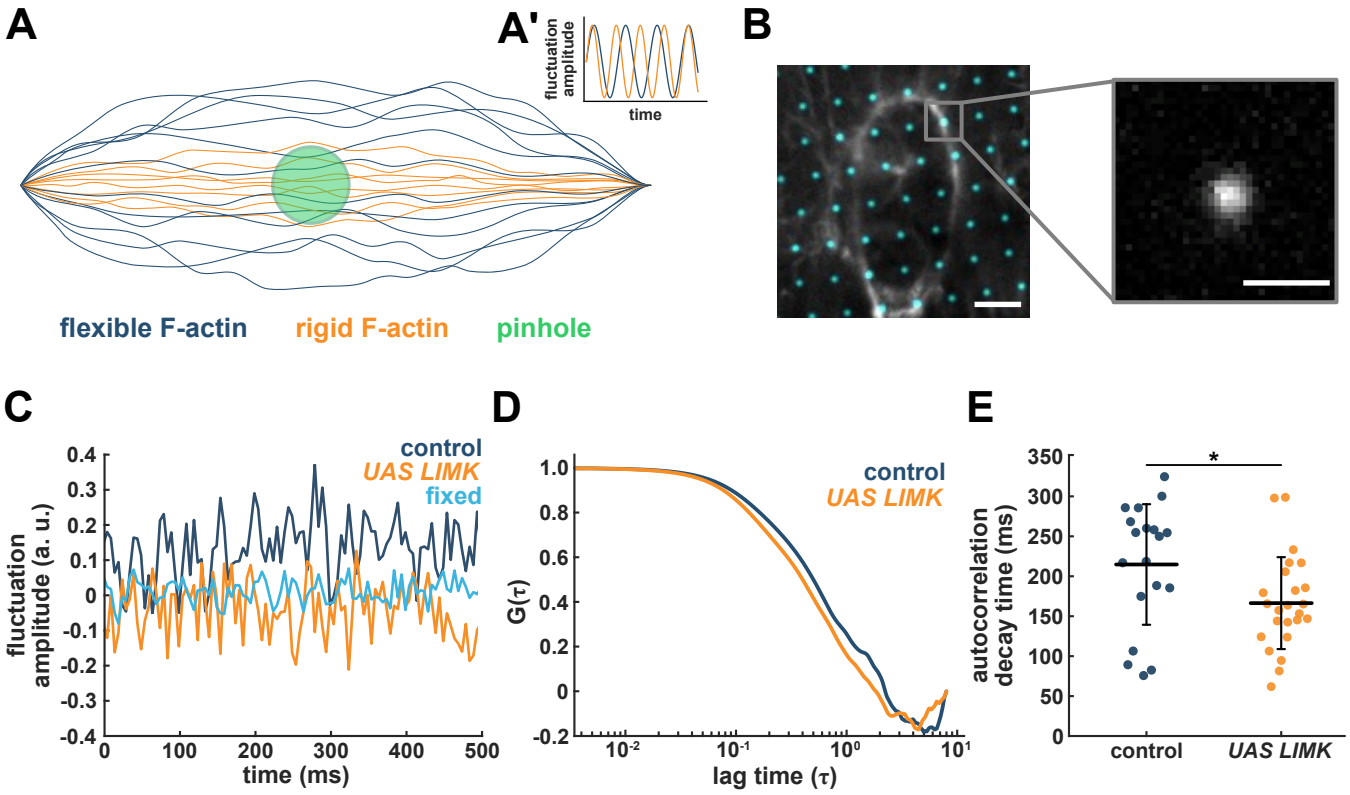

Figure 7. Cofilin controls F-actin rigidity in vivo. (A) Cartoon depicting the impact of F-actin rigidity on thermal fluctuations (A) and fluorescence fluctuations in a diffraction-limited spot (A'). **(B)** F-actin cable around a wound in an embryo expressing GFP:UtrophinABD and imaged while the disk in a spinning disk confocal rotated (grayscale); and arrested disk pinholes (cyan), with sample signal collected from a pinhole (right). Anterior left, ventral down. Bars, 10 µm (left) and 1 µm (right). **(C)** Representative sample fluorescence fluctuations measured through an arrested spinning disk pinhole in a fixed embryo (cyan), or in living control (blue) and LIMK-overexpressing (orange) embryos expressing GFP:UtrophinABD. **(D-E)** Mean autocorrelation, *G*, (D) and autocorrelation decay times (E) for GFP:UtrophinABD fluctuations at the wound edge in control (blue, $n = 19$ pinholes in 13 wounds) and LIMK-overexpressing embryos (orange, $n = 24$ pinholes in 18 wounds). Error bars, SD; line, mean. * $P < 0.05$ (Mann-Whitney test).